Prediction of pressure-induced superconductivity in the ternary systems $YScH_{2n}$ ($n = 3$–6)

Lan-Ting Shi,[1,2,*] Jian-Guo Si,[1,2,*] Robin Turnbull,[3] Akun Liang,[4] Peng-Fei Liu,[1,2] and Bao-Tian Wang[1,2,5,†]

[1]*Institute of High Energy Physics, Chinese Academy of Sciences, Beijing 100049, China*

[2]*Spallation Neutron Source Science Center, Dongguan 523803, China*

[3]*Departamento de Ftsica Aplicada-ICMUV-MALTA Consolider Team, Universitat de Valncia, c/Dr. Moliner 50, Burjassot (Valencia) 46100, Spain*

[4]*Center for Science at Extreme Conditions, University of Edinburgh, Edinburgh EH9 3FD, United Kingdom*

[5]*Collaborative Innovation Center of Extreme Optics, Shanxi University, Taiyuan, Shanxi 030006, China*

(Received 23 August 2023; revised 7 January 2024; accepted 2 February 2024; published 16 February 2024)

Hydrogen-rich ternary compounds are promising candidates for realizing room-temperature superconductivity due to the synergistic effects of crystal structure and electronic properties under high-pressure conditions. Here, the high-pressure structures, electronic properties, and superconductivity of the ternary $YScH_{2n}$ ($n = 3$–6) system are investigated by using the prediction method of particle swarm optimization structure combined with first-principles calculations. We find four stable structures, each with different hydrogen sublattices: $Pm\bar{3}$-$YScH_6$, $P4/mmm$-$YScH_8$, $Cmmm$-$YScH_{10}$, and $Pm\bar{3}m$-$YScH_{12}$. All these $YScH_{2n}$ structures are predicted to be high-temperature superconductors. The electron local function (ELF) results indicate a lack of interaction between hydrogen atoms in $YScH_6$, while the weak H-H covalent interactions are observed in the other stoichiometric ratios. Strikingly, $YScH_6$ maintains dynamic stability down to ambient pressure and keeps a high superconducting critical temperature (T_c) of 66 K. At 140 GPa, the pressure-stabilized $YScH_8$ and $YScH_{10}$ structures exhibit high T_c of 110 and 116 K, respectively. Upon further increasing the content of hydrogen, the lowest dynamically stable pressure of $YScH_{12}$ is increased to 200 GPa, and the calculated T_c is up to 179 K. In all $YScH_{2n}$ structures, $Pm\bar{3}$-$YScH_6$ (stabled from 1 atm to 47 GPa), $P4/mmm$-$YScH_8$ and $Cmmm$-$YScH_{10}$ (stabled from 140 to 250 GPa), $Pm\bar{3}m$-$YScH_{12}$ (stabled from 200 to 286 GPa), strong electron-phonon coupling (EPC) and large electronic density of states of hydrogen at the Fermi level play important roles in their high-temperature superconductivity. It is discussed that phonon softening in the midfrequency region induced mainly by Fermi surface nesting effectively enhances the EPC. In this paper, we potentially discover high-temperature superconducting hydrides that can be stable at atmospheric pressure, taking an important step toward understanding the superconductivity and structural stability of ternary hydrides.

DOI: 10.1103/PhysRevB.109.054512

I. INTRODUCTION

Achieving room-temperature superconductivity has been one of the principal goals of condensed matter physics for a long time [1,2]. Within the framework of Bardeen-Cooper-Schrieffer (BCS) theory, metallic hydrogen has famously been predicted to be a good candidate to achieve superconductivity at room temperature [3–6]. However, experimental metallization of hydrogen remains extremely challenging, requiring very high pressure on a highly compressible sample which is difficult to obtain and maintain. Therefore, despite many independent investigations, the behavior of hydrogen >400 GPa remains disputed [6–10].

Alternatively, it has been suggested by Ashcroft [11] that hydrogen-rich compounds may exhibit similar characteristics to pure hydrogen at lower pressures due to chemical precompression. Extensive studies have shown that compressed hydrogen-rich compounds are potential high-temperature and allegedly room-temperature superconductors, in which the large electronic density of states (DOS) driven by hydrogen and strong electron-phonon coupling (EPC) dominate the superconductivity. Currently, almost all binary hydrides have been extensively studied in theory, and a considerable number have been experimentally confirmed. For example, covalent hydride H_3S [12–15] and clathrate hydrides CaH_6 [16–18], YH_6 [19–22], and LaH_{10} [22–25] have been synthesized >150 GPa and exhibit superconducting transition temperatures (T_c) >200 K. These successful theoretical and experimental research results on binary hydrides have further promoted the development of hydrides under high pressure, with focus now turning to the exploration of ternary and quaternary hydrides.

Recently, the near-ambient superconductivity in a N-doped lutetium hydride has been reported in experiments [26], triggering heated debate. Nonetheless, Ref. [26] strongly proves that ternary hydrides are a series of promising materials for realizing room-temperature superconductivity. In fact, over recent years, the research results on ternary hydrides are

*These authors contributed equally to this work.

†Corresponding author: wangbt@ihep.ac.cn

incrementally increasing the record value of T_c. Ternary hydrides constructed by adding light elements to binary hydrides are a commonly followed synthesis route to achieve a higher superconductivity transition temperature or lower stability pressure. For example, the lithium-doped magnesium hydride MgH_{16} forms a ternary compound Li_2MgH_{16} with a remarkably high estimated T_c of 473 K at 250 GPa [27]. Additionally, Sun *et al*. [28] predicted three high-temperature superconductors in stable ternary lithium-doped rare-earth superhydides [28]. In addition, some metal atoms with similar atomic radii and electronegativity can share the hydrogen sublattice, forming alloy hydrides in the form of solid solutions, which exhibit good stability and superconductivity, such as ternary clathrate hydrides $YCaH_{12}$ [29–31], $ScCaH_{12}$ [32], $YLuH_{12}$ [33], and Y-Zr-H [34]. In addition, a series of La-Y-H compounds have been successfully synthesized by experiment [35]. These important discoveries in ternary hydrides greatly encourage our further exploration, especially ternary hydrides containing rare-earth elements.

Wei *et al.* [36] focused on exploring the structures and high-pressure phase diagrams of Y-Sc-H ternary compounds with various $ScYH_x$ (x = 1–4, 6, 8) compositions. The results indicate that $Pm\bar{3}$-$YScH_6$ is dynamically stable under pressure as low as 0.01 GPa. In addition, Sukmes *et al*. [37] theoretically reported the stable structure of symmetrically Sc/Y-substituted hexahydride $Sc_{0.5}Y_{0.5}H_6$, and the results indicate that this system is a potential high-temperature superconductor under high pressure. However, we believe that the Y-Sc-H system should be able to form more ternary hydrides with higher hydrogen content or under mild pressures due to the abundant binary hydrides of Sc-H [38,39] and Y-H [19–22] predicted. Previous studies [40] have shown that hydrides with high symmetry have more potential to be superconductors with high T_c. Therefore, in this paper, we further systematically calculate the structures and properties of the Y-Sc-H system under different pressures, with a focus on high content of hydrogen. In ternary hydrides $YScH_{2n}$ (n = 3–6), we found four dynamically stable superconducting structures. One of the structures, $Pm\bar{3}$-$YScH_6$, maintains dynamic stability down to ambient pressure and still exhibits superconductivity, which encourages experimental synthesis in the future. The other three structures, $P4/mmm$-$YScH_8$, $Cmmm$-$YScH_{10}$, and $Pm\bar{3}m$-$YScH_{12}$, are clathrate hydrides with predicted T_c values up to 110, 116, and 179 K at high pressures, respectively. Significantly, the T_c of $YScH_6$ reaches 66 K at 1 atm, and further calculation results show that the Fermi surface nesting effectively enhances the EPC. Such a high value of T_c at ambient pressure in metal hydrides is very rare, which provides guidance for future theoretical and experimental work to search for high-temperature superconductors.

II. COMPUTATIONAL DETAILS

In this paper, the stable $YScH_{2n}$ (n = 3–6) compounds were predicted by the particle swarm optimization algorithm CALYPSO [41,42]. We performed 1–4 formula units for $YScH_{2n}$ (n = 3, 4) and 1–2 formula units for $YScH_{2n}$ (n = 5, 6) in the pressure range of 0–400 GPa. Structural relaxations, electronic properties, and total energies were determined in the framework of density functional theory with Perdew-Burke-Ernzerhof parameterization of the generalized gradient approximation as implemented in VASP [43]. Ion-electron interactions were described using the projector augmented-wave method [44], with 1s, 3p4s3d, and 4s4p5s4d as valence electrons for H, Sc, and Y, respectively. A plane-wave energy cutoff of 1000 eV was used. Monkhorst-Pack meshes for Brillouin zone sampling with resolutions of 7×7×7 were employed for thermodynamic calculations and electronic property determination.

Phonon dispersion calculations were performed using the supercell method with PHONOPY [45] and density functional perturbation theory (DFPT) in the QUANTUM ESPRESSO (QE) package [46]. Further EPC calculations were carried out using DFPT as implemented in the QE package [46], where the ultrasoft pseudopotentials for Y, Sc, and H with a kinetic energy cutoff of 60 Ry were employed. The 5×5×5 q-point meshes in the first Brillouin zone were used in the EPC calculation for $YScH_{2n}$ (n = 3–6). Correspondingly, Monkhorst-Pack grids of 20×20×20 were used to ensure k-points sampling convergence with Gaussian width of 0.05 Ry. The superconducting critical temperature T_c was estimated via the Allen-Dynes-modified McMillan formula [47] with correction as follows:

$$T_c = \frac{f_1 f_2 \omega_{\log}}{1.2} \exp\left[-\frac{1.04(1+\lambda)}{\lambda - \mu^* - 0.62\lambda\mu^*}\right], \tag{1}$$

where the μ^* is the effective Coulomb repulsion, f_1 and f_2 are the strong coupling and shape correction factors, respectively, f_1 and f_2 are defined as

$$f_1 = \sqrt[3]{1 + \left[\frac{\lambda}{2.46(1+3.8\mu^*)}\right]^{3/2}}, \tag{2}$$

$$f_2 = 1 + \frac{\left(\frac{\bar{\omega}_2}{\omega_{\log}} - 1\right)\lambda^2}{\lambda^2 + \left[1.82(1+6.3\mu^*)\left(\frac{\bar{\omega}_2}{\omega_{\log}}\right)\right]^2}, \tag{3}$$

where $\bar{\omega}_2$ is the second moment of the normalized weight function, defined as

$$\bar{\omega}_2 = \sqrt{\frac{2}{\lambda}\int^{\omega} \alpha^2 F(\omega) d\omega}. \tag{4}$$

The EPC parameter λ and the logarithmic average frequency $\omega_{\log}$ are calculated as follows:

$$\lambda(\omega) = 2\int \frac{\alpha^2 F(\omega)}{\omega} d\omega. \tag{5}$$

$$\omega_{\log} = \exp\left[\frac{2}{\lambda}\int \frac{d\omega}{\omega}\alpha^2 F(\omega)\ln\omega\right]. \tag{6}$$

Here, the Eliashberg spectral function $\alpha^2 F(\omega)$ is calculated according to the following formula:

$$\alpha^2 F(\omega) = \frac{1}{2\pi N(E_F)} \sum_{qv} \delta(\omega - \omega_q v) \frac{\gamma_{qv}}{\hbar\omega_{qv}}, \tag{7}$$

where ω_{qv} are phonon frequencies, and γ_{qv} is the phonon linewidth as described by

$$\gamma_{qv} = 2\pi\omega_{qv} \sum_{ij} \int \frac{d^3k}{\Omega_{BZ}} |g_{qv}(k,i,j)|^2 \times \delta(\varepsilon_{q,i} - \varepsilon_F)\delta(\varepsilon_{k+q,j} - \varepsilon_F). \tag{8}$$

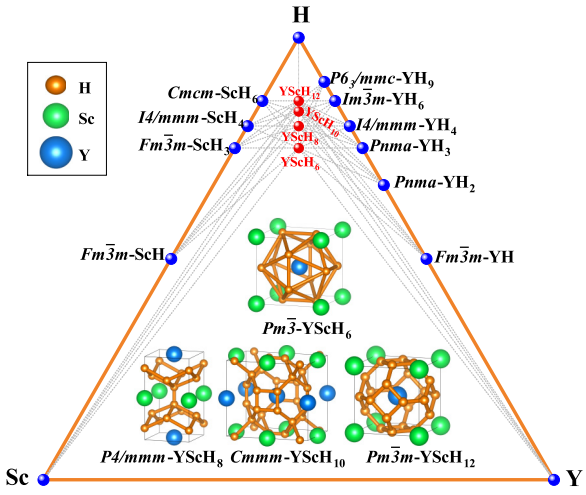

FIG. 1. Ternary phase diagram of the $YScH_{2n}$ ($n = 3$–6) system. The blue dots denote element or binary hydrides, and red dots denote ternary hydrides studied in this paper. The inserted structures are the stable unit cells of $Pm\bar{3}$-$YScH_6$, $P4/mmm$-$YScH_8$, $Cmmm$-$YScH_{10}$, and $Pm\bar{3}m$-$YScH_{12}$.

Here, $g_{qv}(k, i, j)$ is the matrix of the EPC, and $\varepsilon_{q,i}$ is the electronic energy.

III. RESULTS AND DISCUSSION

We perform the random structure searches for the ternary $YScH_{2n}$ ($n = 3$–6) systems at 200 GPa using the CALYPSO code [41,42]. Four ground-state structures with different hydrogen cage configurations are obtained, as shown in Fig. 1. For the vertices of this triangle, we use $P6_222$ for Y [48], $Fm\bar{3}m$ for Sc [49], and $C2/c$ for H_2 [50]. On the edges of the triangle, the reported high-pressure yttrium hydrides (YH, YH_2, YH_3, YH_4, YH_6, and YH_9) and scandium hydrides (ScH, ScH_3, ScH_4, and ScH_6) are shown. No stable Y-Sc alloys have been reported. The stable ternary structures, $Pm\bar{3}$-$YScH_6$, $P4/mmm$-$YScH_8$, $Cmmm$-$YScH_{10}$, and $Pm\bar{3}m$-$YScH_{12}$, are inside the triangular phase diagram. The gray dotted line inside the triangle illustrates the theoretical possible synthesis path of those ternary systems. Moreover, the structural parameters at different pressures of these systems are listed in Table S1 in the Supplemental Material [51], which can be used in further experimental and theoretical works. The volumes and lattice parameters of these four structures as functions of pressure are shown in Figs. S1 and S2 in the Supplemental Material [51], respectively. Clearly, their volumes and lattice parameters gradually decrease with the increase of pressure.

To further ascertain the thermodynamic stability of the $YScH_{2n}$ ($n = 3$–6) system, we calculated the relative enthalpy of all possible decomposition products, as shown in Figs. S3–S6 in the Supplemental Material [51]. In our calculations, we use $P6_222$ for Y [48], $Fm\bar{3}m$ for Sc [48], $P6_3/m$ and $C2/c$ for H_2 [50], $Pnma$ for YH_2, $Pnma$ for YH_3, $I4/mmm$ for YH_4, $Im\bar{3}m$ for YH_6, $P6_3/mmc$ for YH_9, $Fm\bar{3}m$ for YH_{10} [22], $Fm\bar{3}m$ for ScH, $Fm\bar{3}m$ for ScH_3, $I4/mmm$ For ScH_4, and $Cmcm$ for ScH_6 [38,39]. As shown in Figs. S3–S6 in the Supplemental Material [51], after the pressure increasing to 47 GPa, $YScH_6$ easily decomposes into lower-energy binary compounds ScH_3 and YH_3. Nearly all the decomposition products exhibited positive energies of formation relative to $YScH_8$ and $YScH_{10}$ at 111–300 GPa and 129–300 GPa, respectively. For $YScH_{12}$, when the pressure increased to 286 GPa, it was easily decomposed into ScH_6 and YH_6. Therefore, the thermodynamically stable pressure ranges for $YScH_6$, $YScH_8$, $YScH_{10}$, and $YScH_{12}$ are 0–47 GPa, 111–300 GPa, 129–300 GPa, and 195–286 GPa, respectively.

After obtaining the four above structures, their dynamic stability ranges were checked via phonon dispersion curves (see Fig. S7 in the Supplemental Material [51]). The absence of imaginary frequencies suggests that the structures are dynamically stable. Surprisingly, $YScH_6$ is stable at ambient pressure (i.e., 1 atm) and can be continuously stabilized up to 100 GPa. It is worth noting that the stable pressure we predicted is lower than the one calculated by Wei *et al.* [36]. Compared with their results, the different stable pressure may be attributed to the fact that we selected higher-precision calculation parameters. In addition, the $Pm\bar{3}$-$YScH_6$ structure belongs to the A15-type hydrides [52]. A previous study has shown that a similar system ($YZrH_6$) [34] can also be stable at ambient pressure. Both $YScH_8$ and $YScH_{10}$ are stable in the pressure range of 140–250 GPa, while the stability of $YScH_{12}$ requires a higher pressure of 200 GPa due to its higher hydrogen content. After considering thermodynamic and dynamic stability, $YScH_6$ is stable between 0 and 47 GPa, $YScH_8$ is stable between 140 and 250 GPa, $YScH_{10}$ is stable between 140 and 250 GPa, and $YScHYScH_{12}$ is stable between 195 and 286 GPa. As expected, the higher hydrogen content of the rare-earth metal ternary hydrides system tends to require higher stabilizing pressure.

Previous studies have shown that hydrogen cage structures in hydrogen-rich compounds play an important role in electron-phonon interaction [16,24,25]. Here, we calculate the H-H distance in the hydrogen cage configurations as a function of pressure. As shown in Fig. 2(a), the H-H distance in $YScH_6$ is >2 Å, which is much larger than the standard H-H covalent distance in ambient-pressure H_2 (0.74 Å). This clearly indicates the absence of interaction between hydrogen atoms in $YScH_6$, which is also supported by our electron localization function (ELF) calculations. The H atoms form a hydrogen cage with 12 isosceles triangles and eight equilateral triangles, and the bond lengths gradually decrease upon compression.

The shape of the hydrogen cage in $YScH_8$ is the same as that in $ScCaH_8$ [32], consisting of four hexagons and eight rhombuses [see in Fig. 2(b)]. However, it is worth noting that the sizes of the hydrogen cage surrounding the Y and Sc atoms are different. The hexagonal side lengths a and c wrap around the Y atoms, while the side lengths b and d wrap around the Sc atoms. All H-H distances are <1.6 Å over the stable pressure range. Interestingly, the bond lengths of both c and d bonds increase with increasing pressure, which may imply that the hydrogen cages in $YScH_8$ collapse under sufficient high compression.

The hydrogen cages in both $YScH_{10}$ and $YScH_{12}$ are composed of 24 hydrogen atoms, as shown in Fig. 2, which are similar in configuration to the hydrogen cages of CaH_6 [16]

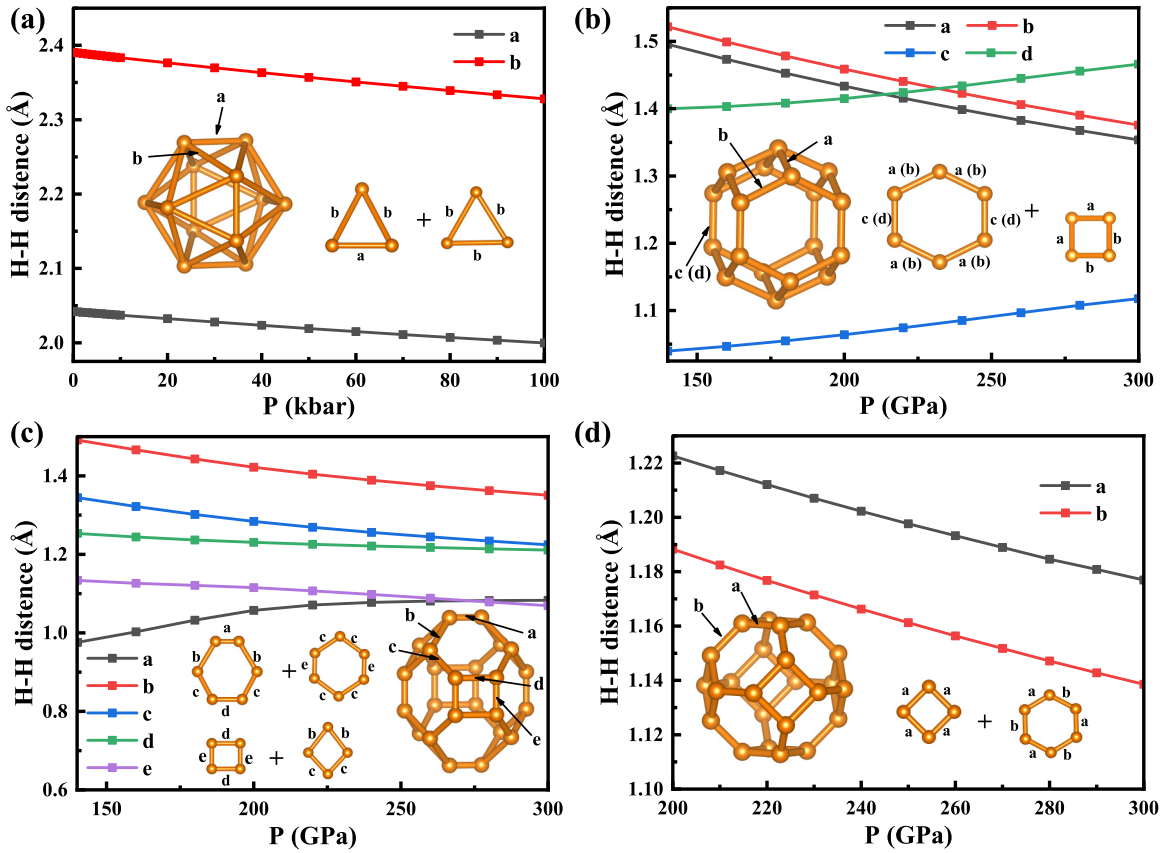

FIG. 2. H-H distances as a function of pressure for (a) $Pm\bar{3}$-$YScH_6$, (b) $P4/mmm$-$YScH_8$, (c) $Cmmm$-$YScH_{10}$, and (d) $Pm\bar{3}m$-$YScH_{12}$. The inset structures show the hydrogen-cage configurations for each of the corresponding structures.

and YH_{10} [22]. They are both composed of quadrilaterals and hexagons. However, due to different types of metal atoms encapsulated, their cage shapes are also different. The different symmetry and stoichiometric ratio result in the H cage in $YScH_{10}$ being more complex. The H24 cage of $YScH_{10}$ consists of two types of hexagons (four of each), two rectangles, and four rhombuses. Except for bond a, which increases upon compression, the rest of the bond lengths decrease with increasing pressure, and all bond lengths are <1.5 Å in the studied pressure range. The H24 cage of $YScH_{12}$ is the same as the H cage in common ternary alkaline earth metal/rare-earth metal hydrides, such as $ScCaH_{12}$ [32] and $YCaH_{12}$ [29,30]. It consists of six squares (side length a) and eight hexagons (side lengths a and b). The a and b bonds gradually decrease with the increase of pressure, and the bond lengths are all <1.3 Å.

The calculated ELF and Bader charge are used to analyze the chemical bonding. Their common feature is the low ELF values between metal and hydrogen atoms, which confirms the existence of ionic bonds (see Fig. S8 in the Supplemental Material [51]). There is almost no electron localization between the nearest H atoms in $YScH_6$, indicating that hydrogen exists at the atomic state. Bader charge analysis of $YScH_6$ at 1 atm shows that each Sc and Y atom loses charge of 1.63 and 1.69 $|e|$, respectively, and each H atom gains 0.553 $|e|$ charge. The ELF value between the nearest H atoms in $YScH_8$ is $\sim$0.82, indicating the formation of H-H covalent bonds. Bader charge analysis reveals that each Sc and Y atom loses 1.284 and 1.221 $|e|$, respectively, at 140 GPa. Moreover, the ELF value of the nearest H-H bond in $YScH_{10}$ is $\sim$0.9, where each Sc and Y atom transfers electrons 1.18 and 1.48 e to H, respectively, resulting in an H atom gaining 2.66 $|e|$. In addition, the ELF value between H atoms in $YScH_{12}$ is 0.62, where each Sc and Y atom transfers 1.25 electrons to H atoms.

The calculated electronic band structures and projected DOS (PDOS) of four $YScH_{2n}$ compounds in their corresponding least stable pressures are shown in Fig. 3. The overlapping of the valence and conduction bands indicates that they are metallic, and the contributions of the d electrons of Sc and Y to the DOS at the Fermi level are significant. For $YScH_6$, the configuration of its band structure is like $YZrH_6$ [34]. However, due to the downward shift of the Fermi level of $YScH_6$, the proportion of H in the total DOS at the Fermi level is higher than that of $YZrH_6$, which implies that $YScH_6$ would exhibit better superconductivity than $YZrH_6$. As for $YScH_8$, electron pockets near the Fermi level at around the Γ and R points enhance the electronic occupation. In addition, there is an obvious van Hove singularity near the Fermi level at the m point, which can effectively enhance the superconductivity. For $YScH_{10}$, the contribution of hydrogen at the Fermi level increases significantly and is higher than that of the d electrons of the Y and Sc atoms. The band structure of $YScH_{12}$ is like those of $YCaH_{12}$ [29,30] and $ScCaH_{12}$ [32], and the

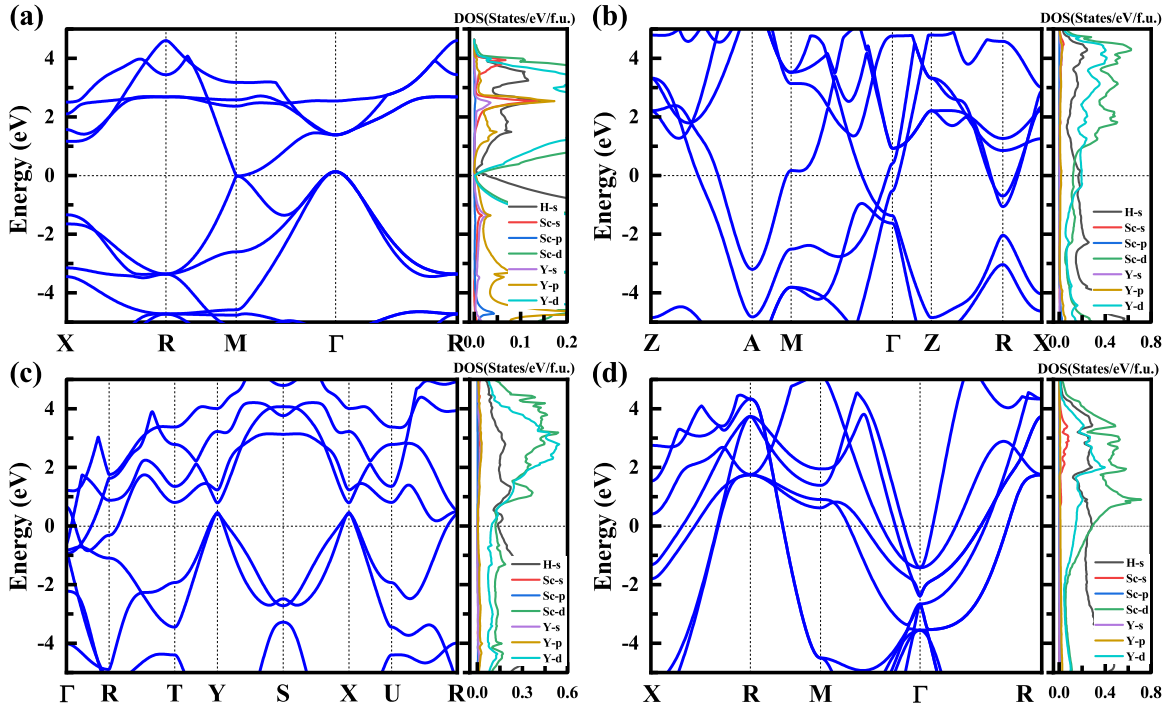

FIG. 3. Calculated electronic band structures and projected density of states (PDOS) for (a) $Pm\bar{3}$-$YScH_6$ at 1 atm, (b) $P4/mmm$-$YScH_8$ at 140 GPa, (c) $Cmmm$-$YScH_{10}$ at 140 GPa, and (d) $Pm\bar{3}m$-$YScH_{12}$ at 200 GPa. The Fermi level is set to zero.

contribution of the H atoms and the d electrons at the Fermi level is close. Furthermore, multiple Fermi pockets exist at m and Γ points near the Fermi level, indicating its good superconductivity. It is well known that the increase of hydrogen content is beneficial to drive the high DOS of hydrogen at the Fermi level, which is also an important prerequisite for hydrides with high T_c, as more electrons will be involved in the formation of Cooper pairs. Therefore, the calculation and analysis of the electronic properties of $YScH_{2n}$ are helpful for our following understanding of their excellent superconductivity.

To explore the superconductivity, we further calculate the phonon dispersion curves, projected phonon DOS (PHDOS), and Eliashberg spectral functions $\alpha^2F(\omega)$ with the electron-phonon integral $\lambda(\omega)$ of the four stable $YScH_{2n}$ and present the results in Fig. 4. As shown, the phonon modes in the low-frequency region are mainly associated with the Sc and Y atoms due to their heavy atomic masses. The lighter H atoms drive the phonon modes in the mid- and high-frequency regions. Note that the high peaks of the Eliashberg spectral function $\alpha^2F(\omega)$ appear in the middle-frequency region, which are mainly caused by the soft phonon modes. In addition, the soft modes on the acoustic branch of $YScH_{2n}$ (n = 3–4) have obvious contributions. For $YScH_6$, the projection of EPC is mainly concentrated on the soft modes around the m and Γ points, especially in the range of 40–80 meV. The calculated $\alpha^2F(\omega)$ and the electron-phonon integral $\lambda(\omega)$ reveal that the low-frequency vibrations (0–40 meV) contribute 33% to the total λ, while the mid-high frequency modes of H atoms contribute 67%. For $YScH_8$, the contribution of the H atoms is ∼48%, and the phonon modes in the low-frequency region mainly related to Sc and Y atoms have a significant contribution to the total λ up to 52%. For $YScH_{10}$, the projection of EPC is mainly concentrated at the Γ point, and the contribution from the mid- and high-frequency region dominated by hydrogen atoms is 58%. The soft mode of optical branch in $YScH_{12}$ is located at the Γ point. The H-dominated DOS at the Fermi level is significant, which also induces strong EPC, and phonon vibrations of hydrogen contribute 74% to the total EPC.

We evaluate the superconducting critical temperatures by solving the Allen-Dynes modified McMillan equation [47] and list the results in Table I. It is worth mentioning that we used strong coupling correction factors f_1 and f_2 to correct T_c values (see in calculation details part), which is conducive to accurate confirmation of the T_c of hydrogen-rich compounds. The Coulomb pseudopotential μ^* is set to 0.1. The total EPC constant λ and logarithmic average phonon frequency $\omega_{\log}$ of $YScH_6$ at 1 atm are 1.31 and 598 K, respectively, and T_c is

TABLE I. Calculated EPC parameter (λ), logarithmic average phonon frequency ($\omega_{\log}$), and critical temperature (T_c) for Y-Sc-H systems at given pressures. A typical value of $\mu^* = 0.1$ is used in this paper.

System	Pressure (GPa)	λ	$\omega_{\log}$	T_c (K)
$YScH_6$	0.001	1.31	598	66.5[a]
$YScH_6$	0.01	0.75	979	32.1[b]
$YScH_8$	140	1.54	817	110.2[a]
$YScH_{10}$	140	1.41	954	116.0[a]
$YScH_{12}$	200	2.18	939	179.3[a]
$Y_{0.5}Sc_{0.5}H_6$	500	1.12	1556	127.0[c]

[a]This paper.
[b]Reference [36].
[c]Reference [37].

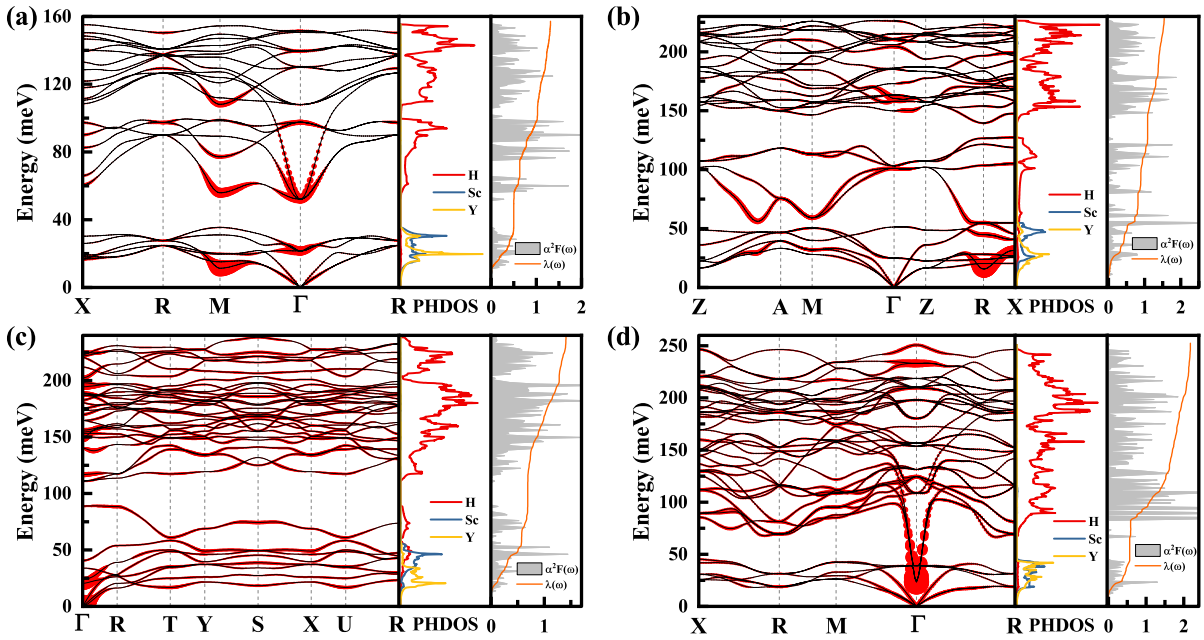

FIG. 4. Calculated phonon dispersion curves, projected phonon density of states, and Eliashberg spectral function $\alpha^2F(\omega)$ together with the electron-phonon integral $\lambda(\omega)$ for (a) $Pm\bar{3}$-$YScH_6$ at 1 atm, (b) $P4/mmm$-$YScH_8$ at 140 GPa, (c) $Cmmm$-$YScH_{10}$ at 140 GPa, and (d) $Pm\bar{3}m$-$YScH_{12}$ at 200 GPa. The size of the red solid dots in the phonon spectra is proportional to the strength of electron-phonon coupling (EPC).

estimated to be 66.5 K. This value is much higher than those of other hydrides of the same type, such as $YZrH_6$ ($T_c = 16$ K at 1 atm) [34] and $ScCaH_6$ ($T_c = 57.3$ K at 200 GPa) [32]. Furthermore, in comparison with those reported by Wei *et al.* [36], our calculations demonstrate that $YScH_6$ not only remains stable under environmental pressures but also exhibits an elevated T_c value. The λ's of $YScH_8$ and $YScH_{10}$ are calculated to be 1.54 and 1.41, respectively, while their T_c values reach 110.2 and 116.0 K at 140 GPa, respectively. Here, $YScH_{12}$ has a strong λ of 2.18 and $\omega_{\log}$ of 939 K at 200 GPa, resulting in a large T_c of 179.3 K. In contrast with the superconducting calculation outcomes for $Y_{0.5}Sc_{0.5}H_6$ at 500 GPa by Sukmas *et al.* [37], the λ and T_c of $YScH_{12}$ are both higher at 200 GPa.

To consider the pressure dependence of the superconducting properties of the system, we calculate the T_c of $YScH_8$, $YScH_{10}$, and $YScH_{12}$ under different pressures (see Fig. S9 in the Supplemental Material [51]). We can see that the T_c of these three structures gradually decreases as the pressure increases. This is mainly caused by the decrease of EPC with increasing of pressure, indicating that the T_c values of these systems are mainly dominated by EPC. Furthermore, the soft mode that causes strong EPC in the mid-frequency region also increases with pressure increase. In addition, we check the influence of the Coulomb potential μ^* on the superconductivity critical temperatures T_c. As shown in Fig. S10 in the Supplemental Material [51], the T_c values of all four structures decrease with increasing values of μ^*. When $\mu^* = 0$, the T_c's of $YScH_6$, $YScH_8$, $YScH_{10}$, and $YScH_{12}$ can reach 72.9, 123.4, 128.3, and 207.3 K, respectively. Obviously, the hydrogen content in the Y-Sc-H system significantly affects the EPC and superconductivity. Both EPC and T_c values increase with increasing hydrogen content. However, the pressure required to stabilize the hydrides also increases with the increasing of the hydrogen content.

To explore the reason for the appearance of the soft phonon modes, we calculate the nesting function $\xi(\mathbf{Q})$ [53] of $YScH_6$ (1 atm):

$$\xi(\mathbf{Q}) = \frac{1}{N}\sum_{k,i,j}\delta(\varepsilon_{k,j} - \varepsilon_F)\delta(\varepsilon_{k+q,j} - \varepsilon_F), \tag{9}$$

where n represents the number of k points, $\varepsilon_{k,j}$ are the Kohn-Sham eigenvalues, ε_F is the Fermi energy, and i, j are the indices of energy bands. The electronic eigenvalues $\varepsilon_{k,j}$ are calculated with a $60\times60\times60$ k-mesh. Figure 5(a) shows the specific value of the nesting function $\xi(\mathbf{Q})$ along high-symmetry lines $X \to R \to m \to \Gamma \to R$ in the Brillouin zone. The large value of nesting function $\xi(\mathbf{Q})$ indicates that Fermi surfaces are more likely to nest along this vector. The nesting function at point Γ in the center of the Brillouin zone represents the entire Fermi surface nesting into itself; its value is the largest but has no specific physical meaning. As shown in Fig. 5(a), the sharp peak of $\xi(\mathbf{Q})$ appears near the m point, demonstrating that strong Fermi surface nesting occurs at this point. In comparison with the distribution of the normalized relative EPC intensity along the high-symmetry path, the EPC intensity coincidentally shows obvious peaks at points Γ and m [see Fig. 5(b)]. There exists optical branch softening at point m in the phonon dispersion curve of $YScH_6$. The strong Fermi surface nesting corresponds to phonon softening at the m point, suggesting that the soft phonon mode is induced by the nesting of the Fermi surface. Notably, the specific values of the nested functions of different paths correspond well to

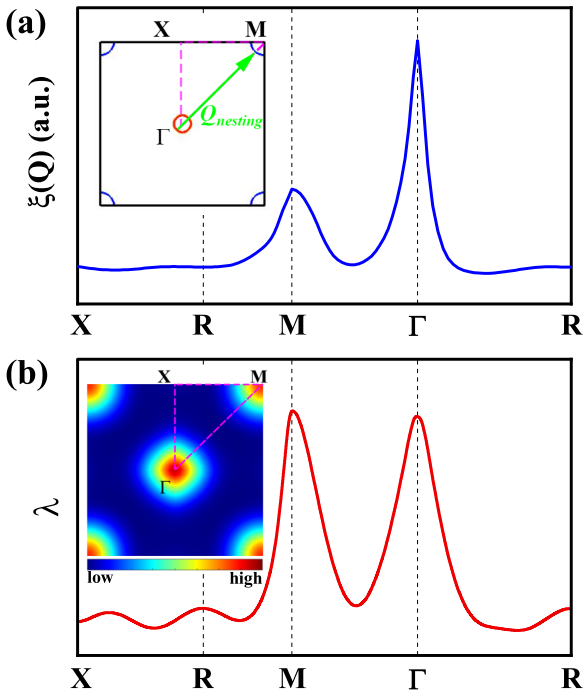

FIG. 5. (a) The calculated nesting unction $\xi(\mathbf{Q})$ and (b) the distribution of normalized relative electron-phonon coupling (EPC) intensity of $Pm\bar{3}$-$YScH_6$ at 1 atm along the high-symmetry path. The inset in (a) is the Fermi surface, and the inset in (b) is the integrated EPC distribution of $YScH_6$ in the plane of $q_z = 0$ at 1 atm.

the number of soft phonon patterns along that direction and the intensity of the phonon softening, which is consistent with previous work on Y_3CaH_{24} [31]. Thus, the Fermi surface nesting is responsible for the soft phonon modes, EPC, and superconductivity.

IV. CONCLUSIONS

In summary, the structures of $YScH_{2n}$ $(n = 3–6)$ ternary hydrides under high pressures were searched using the particle swarm optimization technique combined with density functional theory. Several hydride structures, $Pm\bar{3}$-$YScH_6$, $P4/mmm$-$YScH_8$, $Cmmm$-$YScH_{10}$, and $Pm\bar{3}m$-$YScH_{12}$, which exhibit stability and metallicity between 1 atm and 300 GPa, were predicted and investigated. Interestingly, the $Pm\bar{3}$-$YScH_6$ structure was predicted to be dynamically stable at ambient pressure. As the stoichiometric ratio of hydrogen atoms increases, the pressure required to stabilize the corresponding hydride systems gradually increases. According to our present calculations, $YScH_8$ and $YScH_{10}$ begin to stabilize at 140 GPa, while $YScH_{12}$ requires a higher pressure of 200 GPa. Electronic band structure calculations show that all four encountered structures are metallic under their dynamic stability pressure range. In addition, ELF calculations show that hydrogen atoms in $YScH_6$ have no interaction, while hydrogen atoms in other structures show covalent interactions. Therefore, the hydrogen atoms form hydrogen cage structures in the $YScH_{2n}(n = 4–6)$ systems. This structural evolution caused by increasing the hydrogen content is also concurrent with an increase in T_c. The EPC calculation results show that $YScH_6$ with A15-type structure can maintain dynamic stability down to ambient pressure with T_c up to 66 K, which is larger than the McMillan limit. Increasing the hydrogen content, T_c increases. The large occupation of the electronic DOS of H atoms and the strong interaction between electron and optical phonon modes are the key to obtaining excellent superconductivity in the Y-Sc-H systems. Our comprehensive analysis will provide key insight into the exploration of high-temperature superconductivity in ternary transition metal hydrides.

ACKNOWLEDGMENTS

The authors gratefully acknowledge financial support from the National Natural Science Foundation of China (Grant No. 12074381) and the Guangdong Basic and Applied Basic Research Foundation (Grant No. 2022a1515110404). R.T. acknowledges funding from the Generalitat Valenciana for the postdoctoral Fellowship No. CIAPOS/2021/20.

[1] J. A. Flores-Livas, L. Boeri, A. Sanna, G. Profeta, R. Arita, and M. Eremets, A perspective on conventional high-temperature superconductors at high pressure: Methods and materials, Phys. Rep. **856**, 1 (2020).
[2] I. I. Mazin, Superconductivity: Extraordinarily conventional, Nature (London) **525**, 40 (2015).
[3] J. Bardeen, L. N. Cooper, and J. R. Schrieffer, Theory of superconductivity, Phys. Rev. **108**, 1175 (1957).
[4] N. W. Ashcroft, Metallic hydrogen: A high-temperature superconductor? Phys. Rev. Lett. **21**, 1748 (1968).
[5] J. M. McMahon and D. M. Ceperley, High-temperature superconductivity in atomic metallic hydrogen, Phys. Rev. B **84**, 144515 (2011).
[6] J. M. McMahon, M. A. Morales, C. Pierleoni, and D. M. Ceperley, The properties of hydrogen and helium under extreme conditions, Rev. Mod. Phys. **84**, 1607 (2012).
[7] P. Dalladay-Simpson, R. T. Howie, and E. Gregoryanz, Evidence for a new phase of dense hydrogen above 325 gigapascals, Nature (London) **529**, 63 (2016).
[8] R. P. Dias and I. F. Silvera, Observation of the Wigner-Huntington transition to metallic hydrogen, Science **355**, 715 (2017).
[9] P. Loubeyre, F. Occelli, and P. Dumas, Synchrotron infrared spectroscopic evidence of the probable transition to metal hydrogen, Nature (London) **577**, 631 (2020).
[10] P. Cudazzo, G. Profeta, A. Sanna, A. Floris, A. Continenza, S. Massidda, and E. K. Gross, *Ab initio* description of high-temperature superconductivity in dense molecular hydrogen, Phys. Rev. Lett. **100**, 257001 (2008).
[11] N. W. Ashcroft, Hydrogen dominant metallic alloys: High temperature superconductors? Phys. Rev. Lett. **92**, 187002 (2004).

[12] D. Duan, X. Huang, F. Tian, D. Li, H. Yu, Y. Liu, Y. Ma, B. Liu, and T. Cui, Pressure-induced decomposition of solid hydrogen sulfide, Phys. Rev. B **91**, 180502(R) (2015).

[13] D. Duan, Y. Liu, F. Tian, D. Li, X. Huang, Z. Zhao, H. Yu, B. Liu, W. Tian, and T. Cui, Pressure-induced metallization of dense $(H_2S)_2H_2$ with high-T_c superconductivity, Sci. Rep. **4**, 6968 (2014).

[14] A. P. Drozdov, M. I. Eremets, I. A. Troyan, V. Ksenofontov, and S. I. Shylin, Conventional superconductivity at 203 Kelvin at high pressures in the sulfur hydride system, Nature (London) **525**, 73 (2015).

[15] M. Einaga, M. Sakata, T. Ishikawa, K. Shimizu, M. I. Eremets, A. P. Drozdov, I. A. Troyan, N. Hirao, and Y. Ohishi, Crystal structure of the superconducting phase of sulfur hydride, Nat. Phys. **12**, 835 (2016).

[16] H. Wang, J. S. Tse, K. Tanaka, T. Iitaka, and Y. Ma, Superconductive sodalite-like clathrate calcium hydride at high pressures, Proc. Natl. Acad. Sci. USA **109**, 6463 (2012).

[17] Z. Li, X. He, C. Zhang, X. Wang, S. Zhang, Y. Jia, S. Feng, K. Lu, J. Zhao, J. Zhang *et al.*, Superconductivity above 200 K discovered in superhydrides of calcium, Nat. Commun. **13**, 2863 (2022).

[18] L. Ma, K. Wang, Y. Xie, X. Yang, Y. Wang, M. Zhou, H. Liu, X. Yu, Y. Zhao, H. Wang *et al.*, High-temperature superconducting phase in clathrate calcium hydride CaH_6 up to 215 K at a pressure of 172 GPa, Phys. Rev. Lett. **128**, 167001 (2022).

[19] Y. Li, J. Hao, H. Liu, J. S. Tse, Y. Wang, and Y. Ma, Pressure-stabilized superconductive yttrium hydrides, Sci. Rep. **5**, 9948 (2015).

[20] P. Kong, V. S. Minkov, M. A. Kuzovnikov, A. P. Drozdov, S. P. Besedin, S. Mozaffari, L. Balicas, F. F. Balakirev, V. B. Prakapenka, S. Chariton *et al.*, Superconductivity up to 243 K in the yttrium-hydrogen system under high pressure, Nat. Commun. **12**, 5075 (2021).

[21] I. A. Troyan, D. V. Semenok, G. Kvashnin, A. V. Sadakov, and L. Monacelli, Anomalous high-temperature superconductivity in YH_6, Adv. Mater. **33**, 2006832 (2021).

[22] H. Liu, I. I. Naumov, R. Hoffmann, N. W. Ashcroft, and R. J. Hemley, Potential high-T_c superconducting lanthanum and yttrium hydrides at high pressure, Proc. Natl. Acad. Sci. USA **114**, 6990 (2017).

[23] Z. M. Geballe, H. Liu, A. K. Mishra, M. Ahart, M. Somayazulu, Y. Meng, M. Baldini, and R. J. Hemley, Synthesis and stability of lanthanum superhydrides, Angew. Chem. Int. Ed. **57**, 688 (2018).

[24] A. P. Drozdov, P. P. Kong, V. S. Minkov, S. P. Besedin, M. A. Kuzovnikov, S. Mozaffari, L. Balicas, F. F. Balakirev, D. E. Graf, V. B. Prakapenka *et al.*, Superconductivity at 250 K in lanthanum hydride under high pressures, Nature (London) **569**, 528 (2019).

[25] M. Somayazulu, M. Ahart, A. K. Mishra, Z. M. Geballe, M. Baldini, Y. Meng, V. V. Struzhkin, and R. J. Hemley, Evidence for superconductivity above 260 K in lanthanum superhydride at megabar pressures, Phys. Rev. Lett. **122**, 027001 (2019).

[26] N. Dasenbrock-Gammon, E. Snider, R. McBride, H. Pasan, D. Durkee, N. Khalvashi-Sutter, S. Munasinghe, S. E. Dissanayake, K. V. Lawler, A. Salamat *et al.*, Evidence of near-ambient superconductivity in a N-doped lutetium hydride, Nature (London) **615**, 244 (2023).

[27] Y. Sun, J. Lv, Y. Xie, H. Liu, and Y. Ma, Route to a superconducting phase above room temperature in electron-doped hydride compounds under high pressure, Phys. Rev. Lett. **123**, 097001 (2019).

[28] Y. Sun, Y. Wang, X. Zhong, Y. Xie, and H. Liu, High-temperature superconducting ternary Li-*R*-H superhydrides at high pressures (R = Sc, Y, La), Phys. Rev. B **106**, 024519 (2022).

[29] X. Liang, A. Bergara, L. Wang, B. Wen, Z. Zhao, X.-F. Zhou, J. He, G. Gao, and Y. Tian, Potential high-T_c superconductivity in $CaYH_{12}$ under pressure, Phys. Rev. B **99**, 100505(R) (2019).

[30] H. Xie, D. Duan, Z. Shao, H. Song, Y. Wang, X. Xiao, D. Li, F. Tian, B. Liu, and T. Cui, High-temperature superconductivity in ternary clathrate $YCaH_{12}$ under high pressures, J. Phys.: Condens. Matter **31**, 245404 (2019).

[31] W. Zhao, D. Duan, M. Du, X. Yao, Z. Huo, Q. Jiang, and T. Cui, Pressure-induced high-T_c superconductivity in the ternary clathrate system Y-Ca-H, Phys. Rev. B **106**, 014521 (2022).

[32] L.-T. Shi, Y.-K. Wei, A. K. Liang, R. Turnbull, C. Cheng, X.-R. Chen, and G.-F. Ji, Prediction of pressure-induced superconductivity in the novel ternary system $ScCaH_{2n}$(n = 1–6), J. Mater. Chem. C **9**, 7284 (2021).

[33] M. Du, H. Song, Z. Zhang, D. Duan, and T. Cui, Room-temperature superconductivity in Yb/Lu substituted clathrate hexahydrides under moderate pressure, Research **2022**, 0001 (2022).

[34] W. Zhao, H. Song, M. Du, Q. Jiang, T. Ma, M. Xu, D. Duan, and T. Cui, Pressure-induced high-temperature superconductivity in ternary Y-Zr-H compounds, Phys. Chem. Chem. Phys. **25**, 5237 (2023).

[35] D. V. Semenok, I. A. Troyan, A. G. Ivanova, A. G. Kvashnin, I. A. Kruglov, M. Hanfland, A. V. Sadakov, O. A. Sobolevskiy, K. S. Pervakov, I. S. Lyubutin *et al.*, Superconductivity at 253 K in lanthanum-yttrium ternary hydrides, Mater. Today **48**, 18 (2021).

[36] Y. K. Wei, L. Q. Jia, Y. Y. Fang, L. J. Wang, Z. X. Qian, J. N. Yuan, G. Selvaraj, G. F. Ji, and D. Q. Wei, Formation and superconducting properties of predicted ternary hydride $ScYH_6$ under pressures, Int. J. Quantum Chem. **121**, e26459 (2020).

[37] W. Sukmas, P. Tsuppayakorn-aek, U. Pinsook, R. Ahuja, and T. Bovornratanaraks, Roles of optical phonons and logarithmic profile of electron-phonon coupling integration in superconducting $Sc_{0.5}Y_{0.5}H_6$ superhydride under pressures, J. Alloys Compd. **901**, 163524 (2022).

[38] X. Ye, R. Hoffmann, and N. W. Ashcroft, Theoretical study of phase separation of scandium hydrides under high pressure, J. Phys. Chem. C **119**, 5614 (2015).

[39] X. Ye, N. Zarifi, E. Zurek, R. Hoffmann, and N. W. Ashcroft, High hydrides of scandium under pressure: Potential superconductors, J. Phys. Chem. C **122**, 6298 (2018).

[40] E. Zurek and T. Bi, High-temperature superconductivity in alkaline and rare earth polyhydrides at high pressure: A theoretical perspective, J. Chem. Phys. **150**, 050901 (2019).

[41] Y.-C. Wang, J. Lv, L. Zhu, and Y.-M. Ma, CALYPSO: A method for crystal structure prediction, Comput. Phys. Commun. **183**, 2063 (2012).

[42] Y.-C. Wang, J. Lv, L. Zhu, and Y.-M. Ma, Crystal structure prediction via particle-swarm optimization, Phys. Rev. B **82**, 094116 (2010).

[43] G. Kresse and J. Furthm¨ıller, Efficient iterative schemes for *ab initio* total-energy calculations using a plane-wave basis set, Phys. Rev. B **54**, 11169 (1996).

[44] P. E. Blöchl, Projector augmented-wave method, Phys. Rev. B **50**, 17953 (1994).

[45] A. Togo and I. Tanaka, First principles phonon calculations in materials science, Scr. Mater. **108**, 1 (2015).

[46] P. Giannozzi, S. Baroni, N. Bonini, M. Calandra, R. Car, C. Cavazzoni, D. Ceresoli, G. L. Chiarotti, M. Cococcioni, I. Dabo *et al.*, QUANTUM ESPRESSO: A modular and open-source software project for quantum simulations of materials, J. Phys.: Condens. Matter **21**, 395502 (2009).

[47] P. B. Allen and R. C. Dynes, Transition temperature of strong-coupled superconductors reanalyzed, Phys. Rev. B **12**, 905 (1975).

[48] Y. Chen, Q. M. Hu, and R. Yang, Predicted suppression of the superconducting transition of new high-pressure yttrium phases with increasing pressure from first-principles calculations, Phys. Rev. Lett. **109**, 157004 (2012).

[49] D. R. Kammler, M. A. Rodriguez, R. G. Tissot, D. W. Brown, B. Clausen, and T. A. Sisneros, *In-situ* time-of-flight neutron diffraction study of high-temperature α-to-β phase transition in elemental scandium, Metall. Mater. Trans. A **39**, 2815 (2008).

[50] C. J. Pickard and R. J. Needs, Structure of phase III of solid hydrogen, Nat. Phys. **3**, 473 (2007).

[51] See Supplemental Material at http://link.aps.org/supplemental/10.1103/PhysRevB.109.054512 for Fermi surface and pressure dependences of volume, lattice parameters, enthalpy differences, T_c, and electron-phonon coupling as well as phonon dispersions, electron localization functions, and structural parameters at different pressures.

[52] X. Wei, X. Hao, A. Bergara, E. Zurek, X. Liang, L. Wang, X. Song, P. Li, L. Wang, G. Gao *et al.*, Designing ternary superconducting hydrides with A15-type structure at moderate pressures, Mater. Today Phys. **34**, 101086 (2023).

[53] Y. Ma, D. Duan, Z. Shao, H. Yu, H. Liu, F. Tian, X. Huang, D. Li, B. Liu, and T. Cui, Divergent synthesis routes and superconductivity of ternary hydride $MgSiH_6$ at high pressure, Phys. Rev. B **96**, 144518 (2017).